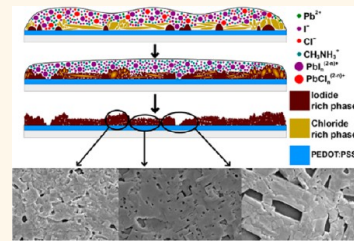


# Role of Chloride in the Morphological Evolution of Organo-Lead Halide Perovskite Thin Films

Spencer T. Williams,<sup>†</sup> Fan Zuo,<sup>†</sup> Chu-Chen Chueh,<sup>†</sup> Chien-Yi Liao,<sup>†</sup> Po-Wei Liang,<sup>†</sup> and Alex K.-Y. Jen<sup>\*,†,‡</sup>

<sup>†</sup>Department of Materials Science and Engineering, University of Washington, Seattle, Washington 98195, United States and <sup>‡</sup>Department of Chemistry, University of Washington, Seattle, Washington 98195, United States

**ABSTRACT** A comprehensive morphological study was used to elucidate chloride's role in  $\text{CH}_3\text{NH}_3\text{PbI}_{3-x}\text{Cl}_x$  film evolution on a conducting polymer, PEDOT:PSS. Complex ion equilibria and aggregation in solution, as well as the role they play in nucleation, are found to ultimately be responsible for the unique morphological diversity observed in perovskite films grown in the presence of the chloride ion. An intermediate phase that is generated upon deposition and initial annealing templates continued self-assembly in the case of  $\text{CH}_3\text{NH}_3\text{PbI}_{3-x}\text{Cl}_x$ . In the absence of chloride, the film growth of  $\text{CH}_3\text{NH}_3\text{PbI}_3$  is directed by substrate interfacial energy. By employing the through-plane TEM analysis, we gain detailed insight into the unique crystallographic textures, grain structures, and elemental distributions across the breadth of films grown from precursor solutions with different chemistries. The lattice coherence seen in morphologies generated under the influence of chloride provides a physical rational for the enhancement in carrier diffusion length and lifetime.



**KEYWORDS:** perovskite · chloride · crystallization mechanism · planar heterojunction · electron diffraction

With the rapid rise in efficiencies reported in the past two years (from 13% to 18%),<sup>1</sup> organo-lead halide perovskite photovoltaics are considered viable competitors for prevailing silicon based technologies. Since the seminal work in 2009 by Miyasaka *et al.* demonstrating this material's potential in photovoltaics<sup>2</sup> and the work of Park *et al.* in 2012 demonstrating a viable high performance device platform,<sup>3</sup> many cell architectures have been explored;<sup>4–9</sup> however, exerting better control over perovskite crystal formation remains the critical challenge in each case.<sup>10–17</sup> Depositing lead iodide ( $\text{PbI}_2$ ) seed crystals into mesoporous  $\text{TiO}_2$  has been demonstrated to effectively improve the quality of resulting perovskite absorber layers in dye sensitized solar cells (DSSCs), which highlights the impact of the nucleation event on the resulting crystallinity of these materials. Film growth in the planar heterojunction (PHJ) architecture has proven to be even more challenging due to the difficulty of encouraging homogeneous crystallization across planar interfaces, especially in the case of solution based techniques.<sup>10,13–15,17–20</sup> Physical vapor deposition

has been demonstrated to be an effective way to grow high quality perovskite films in the PHJ architecture,<sup>21</sup> but in this case, we lose the benefits solution processing offers. Similar to the case of DSSCs, a variety of seeded growth approaches have been investigated to modulate the crystal formation of perovskite thin-films as in the case of dip coated<sup>11</sup> and vapor assisted<sup>12</sup> film development. With regard to manufacturing, developing a simple and low temperature solution based growth process is essential to meet current commercial requirements.

Since Lee *et al.* demonstrated efficient and simultaneous electron and hole transport in a mixed iodide/chloride organo-lead perovskite,<sup>10</sup> many studies have used chloride inclusion in the perovskite precursor solution as an immensely effective method to enhance crystal formation and morphology of perovskite thin-films.<sup>22,23</sup> The resulting electronic properties of such films have been found to be greatly improved, most notable of which are the carrier lifetime and diffusion length which are found to increase by more than an order of magnitude.<sup>24</sup> Great strides in the engineering of efficient PHJ organo-lead halide perovskite solar

\* Address correspondence to  
ajen@u.washington.edu.

Received for review July 29, 2014  
and accepted October 6, 2014.

Published online October 06, 2014  
10.1021/nn5041922

© 2014 American Chemical Society

cells have been made through the incorporation of chloride to improve perovskite morphological development and optoelectronic performance. Significant improvements have been made in systems incorporating chloride either by using the lead chloride<sup>10,14,24,25</sup> ( $\text{PbCl}_2$ ) or methylammonium chloride (MACl) salt.<sup>23</sup> This advance has been integral to the rapid increase of device performance in a variety of architectures, but the underlying mechanism through which such dramatic enhancement is achieved still remains unclear. It is such an important issue that while this work was under revision two serendipitously complementary studies were published that have enabled deepened analysis throughout the following text.<sup>26,27</sup>

There has been increasing discussion in the recent literature as to the final state of the chloride ion in these systems. Initially it was assumed that chloride preferentially occupies axial atomic coordinates in lead halide octahedra at equilibrium after annealing because of a slight contraction observed in the *c*-axis *via* XRD,<sup>21</sup> but the discussion has since shifted to whether the ion remains in the system at all.<sup>18,23,25–29</sup> Colella *et al.* demonstrated that the development of the methylammonium (MA) lead iodide perovskite ( $\text{MAPbI}_3$ ) is thermodynamically preferred over the development of a predominantly lead chloride perovskite lattice ( $\text{MAPbCl}_3$ ). They found that only supplying a stoichiometrically insufficient amount of iodide to the system could ensure the existence of  $\text{MAPbCl}_3$  at equilibrium. In addition, they demonstrate that the solubility limit of chloride in  $\text{CH}_3\text{NH}_3\text{PbI}_{3-x}\text{Cl}_x$  ( $\text{MAPbI}_{3-x}\text{Cl}_x$ ) is quite low and that phase separation readily occurs.<sup>25</sup> As will be discussed, both this study and the recent literature (Tidhar *et al.*<sup>26</sup> and Yu *et al.*<sup>27</sup>) repeatedly show that chloride does not remain in sufficient quantities to measure with the prevailing techniques, which makes the question of chloride's exact influence that much more compelling. In fact, Yu *et al.* demonstrate that without allowing chloride volatilization, neither  $\text{MAPbI}_3$  nor  $\text{MAPbI}_{3-x}\text{Cl}_x$  can be formed.<sup>27</sup> These results do conflict with analogous compositional measurements in the somewhat less recent literature,<sup>23,25,28</sup> and represent a departure from certain prevailing opinions in the field.

In this study, we present a morphological investigation of the organo-lead halide perovskite system ( $\text{CH}_3\text{NH}_3\text{PbX}_3$ , X = I/Cl) by using scanning and transmission electron microscopy (SEM and TEM) to elucidate chloride's role in impacting crystal evolution. We find that the presence of chloride induces a templated topotactic self-assembly driven phase transformation that has striking impacts on the microstructure and orientation of perovskite films, as is revealed through TEM. We also link the rapid formation of this template phase with the generation of composition gradients throughout the evolving film through an examination of the role of dynamic solution equilibria. As far as we

know, this is the first study employing TEM for direct through-plane characterization of perovskite thin films grown under conditions identical to those used for device fabrication in the PHJ architecture. This powerful analysis is capable of probing the crystallographic consequences of film growth like crystalline texture, grain structure, and elemental distribution across the breadth of a film. It both greatly increases insight into the relevant crystal chemistry and may provide direct physical evidence of how chloride inclusion leads to such significantly enhanced carrier lifetimes and diffusion lengths.

## RESULTS AND DISCUSSION

**Addressing Morphological Variety.** When fabricating conventional PHJ devices (ITO/PEDOT:PSS/perovskite/PC<sub>61</sub>BM/electrode)<sup>13</sup> from a precursor solution made with  $\text{PbCl}_2$  (solution stoichiometry of 3MAI +  $\text{PbCl}_2$ ), we often observe a variety of coexisting perovskite film morphologies. However, when the films are grown from a solution made with only the methylammonium iodide (MAI) salt and  $\text{PbI}_2$  (stoichiometry of MAI +  $\text{PbI}_2$ ), films do not show this degree of variety and are almost entirely consistent (Supporting Information Figure S1). SEM micrographs (Figure 1) show the coexistence of three typically dominant morphologies we observe in films grown from precursor solutions of 3MAI +  $\text{PbCl}_2$ , all of which are highlighted in the overview in Figure 1a. We find that a morphology with good coverage but no apparent crystal alignment (Figure 1b), a morphology with dramatic crystal faceting and long-range alignment (Figure 1c), and a morphology with poor coverage (Figure 1d) highly reminiscent of that formed from a precursor solution of MAI +  $\text{PbI}_2$  (Supporting Information Figure S1) dominate  $\text{MAPbI}_{3-x}\text{Cl}_x$  films to differing degrees. In the overview image (Figure 1a), the regions shown in Figure 1b,c often appear bright and dark in contrast, respectively. Given the unique morphological diversity in films grown from solutions prepared with  $\text{PbCl}_2$ , it can be speculated that the mere presence of the chloride ion does not tell the whole story regarding its impact on film evolution and crystal growth.

To determine how the presence of chloride is leading to such uniquely varied morphology, we first considered the possible impacts of coarsening, phase inhomogeneity, and compositional inhomogeneity in the final film. Coarsening is a process in which a crystal's surface is restructured through atomic diffusion to minimize surface energy. If halted before completion, this process could make the observed morphological diversity the result of a transition from a kinetically favored morphology to a thermodynamically favored structure. Eperon *et al.* argue that atomic diffusion becomes negligible after the appropriate stoichiometry has been reached and the majority of solvent has volatilized,<sup>18</sup> but to exclude the possibility

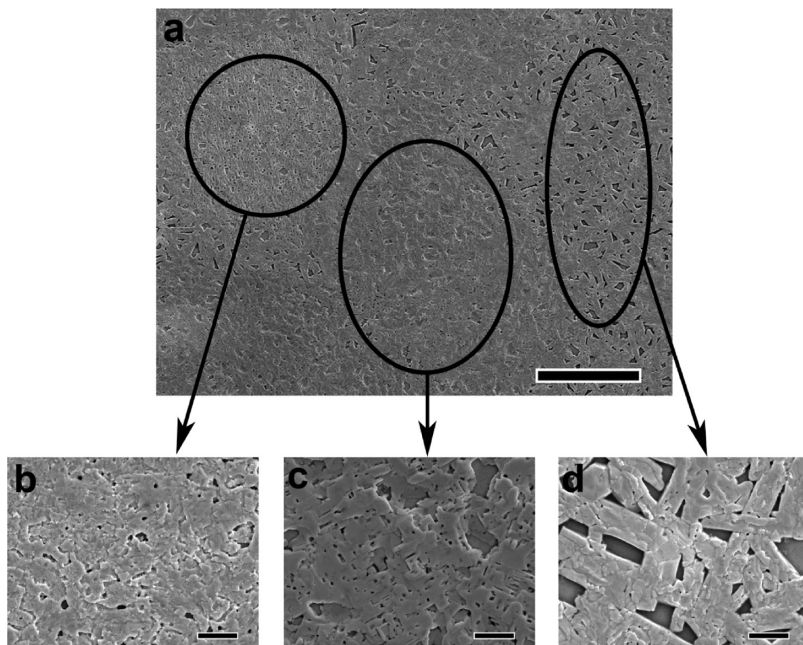


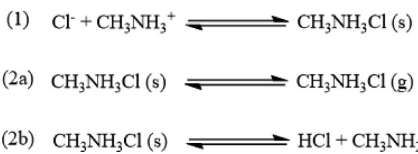
**Figure 1.** Typical  $\text{CH}_3\text{NH}_3\text{PbI}_{3-x}\text{Cl}_x$  thin film grown on PEDOT:PSS through 1-step deposition of 3MAI +  $\text{PbCl}_2$ . (a) Overview in which all three morphologies we observe to consistently dominate these systems are simultaneously visible (scale bar is  $20\ \mu\text{m}$ ). (b–d) Closer views of these three characteristic morphologies (scale bars are  $2\ \mu\text{m}$ ).

that coarsening is contributing to the observed morphological variety, the influence of extended annealing on the distribution of morphologies throughout a 24 h time frame was investigated in both films cast from 3MAI +  $\text{PbCl}_2$  (Supporting Information Figure S2a–f) and MAI +  $\text{PbI}_2$  (Supporting Information Figure S2g–l) solutions. There is no consistent change in the prominence of the areas of poor coverage, dark contrast, and light contrast as annealing time increases in Supporting Information Figure S2a–f, indicating that the suggestion by Eperon *et al.* that diffusion slows to an extent to render further morphological change unfavorable after  $\sim 2$  h is sound.<sup>18</sup> Although Supporting Information Figure S2g–l is shown at a greater magnification because of the lack of morphological diversity, no significant coarsening can be observed in films cast from a MAI +  $\text{PbI}_2$  solution either.

Confirming that coarsening is not the dominant cause of morphological diversity, inhomogeneity in final perovskite composition was considered as a possible culprit. X-ray diffraction (XRD) of a selection of films from the annealing study presented in Supporting Information Figure S2 shows good phase purity with the exception of a small amount of residual  $\text{PbI}_2$  (Supporting Information Figure S4), ruling out phase variation as the main cause of morphological diversity as well. With this in mind, we considered possible variation in chloride content throughout each film, but SEM energy dispersive spectroscopy (EDS) shows no measurable chloride remaining in the bulk of any of the 3MAI +  $\text{PbCl}_2$  films (Supporting Information Table S1). While this echoes a number of other studies,<sup>26,27,29</sup> SEM EDS analysis has great limitations

when analyzing the composition of thin films. These are discussed in detail in Supporting Information Figure S3. Compounding the ambiguity created by the limitation of the technique itself, chloride loss during SEM EDS analysis has been observed by Colella *et al.*,<sup>25</sup> but since the I:Pb ratios in films with and without chloride are almost identical, this is by no means the dominant issue (Supporting Information Table S1). We believe these limitations taken together with the tendency to generate  $\text{PbI}_2$  through extended annealing<sup>16</sup> are responsible for the deviation from the ideal I:Pb ratio observed in both the  $\text{CH}_3\text{NH}_3\text{PbI}_3$  and  $\text{CH}_3\text{NH}_3\text{PbI}_{3-x}\text{Cl}_x$  films, which is collectively  $2.68 \pm 0.15$ , but signal from  $\text{PbI}_2$  in the XRD patterns in Supporting Information Figure S4 is small in comparison to that from the perovskite.

The issue of chloride loss has been raised in recent literature.<sup>16,23,26,27</sup> The currently considered loss pathways center around the sublimation of  $\text{MAI}$ <sup>16,27,30,31</sup> or a degradation of  $\text{MAI}$  into the volatile hydrochloric acid (HCl) and methylamine species facilitated by residual water (Scheme 1).<sup>32</sup> The nature of this loss mechanism suggests that chloride must diffuse to the film's surface to ultimately escape the system, meaning that a bulk sensitive composition measurement like SEM EDS may miss residual chloride remaining at the perovskite's surface. Thus, to complement the EDS data we conducted X-ray photoelectron spectroscopy (XPS), a highly surface sensitive ( $\sim 5$ – $10$  nm) composition analysis technique. As can be readily seen in Supporting Information Figure S5, the signal characteristic of chloride's 2p core electrons is completely absent and only the weak peak from iodide's 4s electrons can be



**Scheme 1. Mechanisms for the Loss of Chloride. Sublimation of Methylammonium Chloride (2a) or Decomposition into Hydrochloric Acid and Methylamine (2b) May Be Responsible for the Loss of Chloride during Film Growth**

observed indicating no chloride remains above the instrument's detection limit.

These measurements, as well as a host of others in the current literature, serve to demonstrate that chloride evolution plays a key role in the phase transformation responsible for lead iodide perovskite growth from solution. They do not, however, exclude entirely the possibility that residual chloride remains in the lattice at high enough concentrations to perturb defect chemistry, molecular order, and electronic behavior.<sup>33,34</sup> While in light of these repeatedly confirmed results Yu *et al.* argue that it is appropriate to adopt the formula  $\text{CH}_3\text{NH}_3\text{PbI}_3$  to define perovskites grown in the presence of chloride,<sup>27</sup> we suggest that the use of the formula  $\text{CH}_3\text{NH}_3\text{PbI}_{3-x}\text{Cl}_x$  remains advantageous because we should not yet neglect the possible impact small amounts of Cl (<0.1 at%) may have on crystal and electronic structure.<sup>33,34</sup> As will be shown, the presence of Cl has a significant impact on perovskite transformation pathway rendering the resulting material structurally and electronically distinct.<sup>24,29,35,36</sup> We will continue to use the formula  $\text{CH}_3\text{NH}_3\text{PbI}_{3-x}\text{Cl}_x$  with the caveat that if  $x$  is non-zero it does not exceed the part per thousand range.

**Addressing the Influence of Solution Chemistry.** Excluding the influences of coarsening, compositional inhomogeneity, and phase inhomogeneity as the primary sources of the observed morphological diversity suggests that final morphology is determined during deposition and initial annealing. This motivates us to evaluate the importance of the various chemical equilibria that occur within the precursor solution before deposition. Until this point, it has generally been thought in the literature that the function of the  $\text{PbCl}_2$  salt is largely to introduce chloride ions into the solution, which ultimately creates competition in ligating  $\text{Pb}^{2+}$  ions upon deposition and thus modifies crystallization kinetics.<sup>23</sup> If this is the case, how we introduce chloride into the system should have no impact upon the final product.

We fabricated two sets of films using solutions with identical overall compositions, but in one we introduced chloride through the  $\text{PbCl}_2$  salt and in the other we introduced chloride through the use of methylammonium chloride (MACl) (Figure 2), similar to the strategy employed by Moore *et al.*<sup>37</sup> The solubilities of  $\text{PbCl}_2$  and MACl differ in dimethylformamide (DMF),

and the presence of MAI markedly increases the solubility of  $\text{PbCl}_2$ . The very soluble MAI quickly dissociates into its component ions which supplies a large amount of  $\text{I}^-$  driving complex ion formation with  $\text{PbCl}_2$  forward in a process similar to the formation of  $\text{PbCl}_4^{2-}$ ,  $\text{PbCl}_3^-$ ,  $\text{PbI}^+$ ,  $\text{PbI}_3^-$ , and  $\text{PbI}_4^{2-}$  in water.<sup>38</sup> The aprotic nature of DMF lends to the stability of more highly coordinated lead ions.<sup>39</sup> Thus, it can be expected that more chloride exists as a ligand in complex lead ions in the solution prepared with  $\text{PbCl}_2$  as compared to the solution prepared with MACl. The use of MACl allows us to supply ionic chloride to the solution without the addition of any potentially problematic spectator ions which is key in isolating the influence of chloride itself.

Figure 2a shows an image of perovskite grown without chloride (MAI +  $\text{PbI}_2$ ) for comparison purposes. The gradual addition of MACl (Figure 2b–e) seems to encourage the development of a morphology reminiscent of the regions shown in Figure 1b, consistent with the observation of Zhao *et al.* that MACl encourages the formation of small closely packed crystallites.<sup>23</sup> In contrast, as we incorporate increasing amounts of  $\text{PbCl}_2$  (Figure 2f–i), we see a gradual shift from the morphology characteristic of MAI +  $\text{PbI}_2$  to the morphology characteristic of Figure 1c. In all cases except the case of 3MAI +  $\text{PbCl}_2$  (Figure 1), morphology throughout the film is largely homogeneous beyond the micrometer scale (Supporting Information Figure S6). As such, Figure 2i is included purely to facilitate discussion as it alone is not completely representative of the morphological variety found in systems grown from 3MAI +  $\text{PbCl}_2$  (Figure 1).

As  $\text{PbCl}_2$  content increases in Figure 2f–h, we can see the gradual development of the sharply faceted crystalline domains interconnected at precise right angles that are characteristic of the morphology shown in Figures 1c and 2i. Furthermore, this morphological feature is only observed in systems grown from solutions made with  $\text{PbCl}_2$  as opposed to those grown without chloride (Figure 2a) and films grown from solutions with MACl (Figure 2b–e). The other dominant morphologies observed in films cast from 3MAI +  $\text{PbCl}_2$  solutions (Figure 1d,b) bear great similarity to films grown from solutions of MAI +  $\text{PbI}_2$  and 2MACl + MAI +  $\text{PbI}_2$  (Figures 2a,e), respectively. This implicates variations in local chemistry throughout an evolving film as the cause of the unique morphological diversity observed upon chloride inclusion. This tracks well with the generation of composition gradients upon the formation of the intermediate phase. From a crystal growth perspective, this suggests that halide composition is a key factor in determining the nature of the nucleation event. It is worth noting that film coverage improves greatly upon the inclusion of chloride in the case of both MACl and  $\text{PbCl}_2$ . All films exhibit good phase purity (Supporting Information Figure S7).

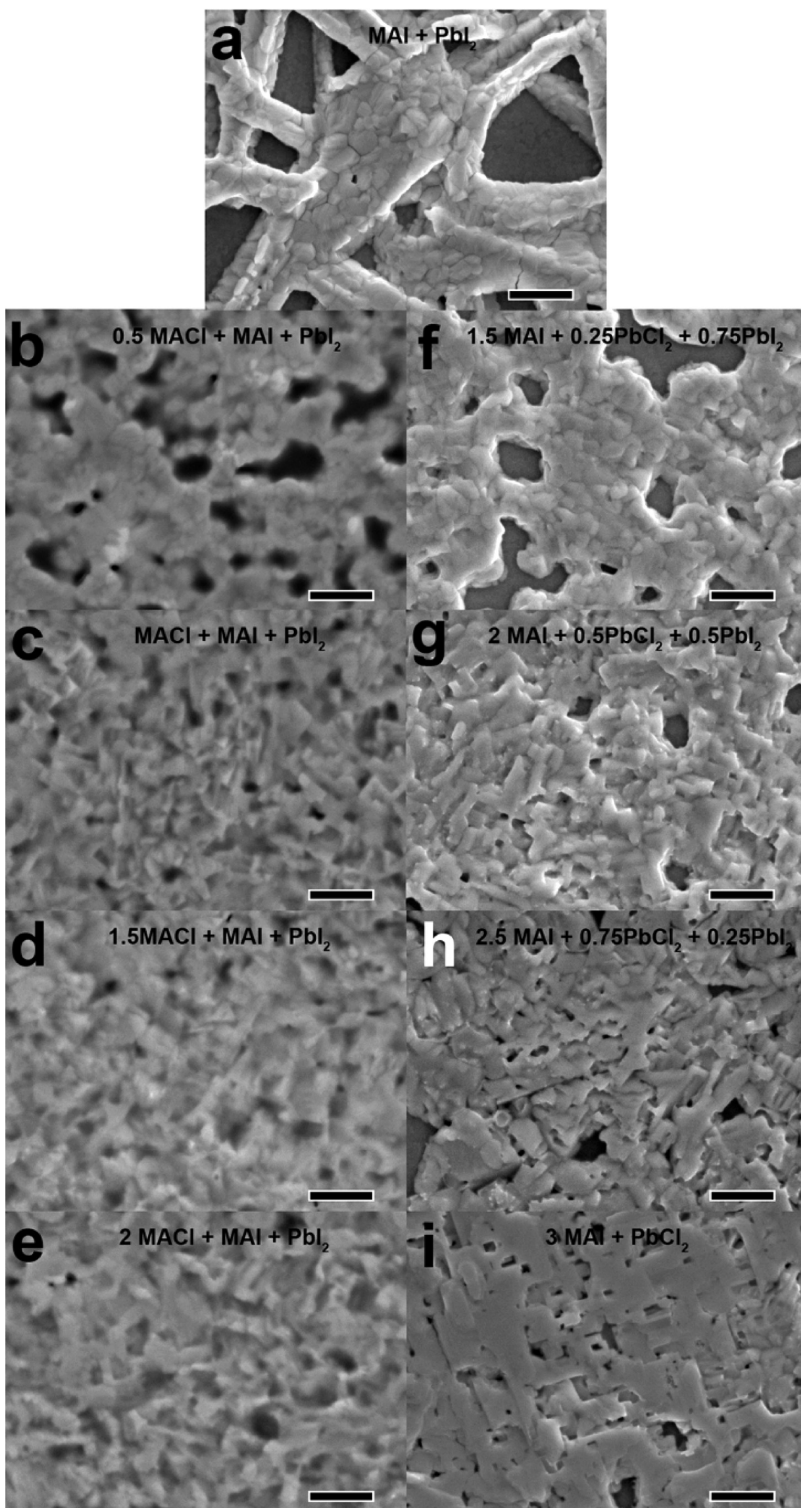


**Figure 2. Impact of solution chemistry on  $\text{MAPbI}_{3-x}\text{Cl}_x$  film growth:** (a) grown from a solution with the stoichiometry  $\text{MAI} + \text{PbI}_2$ ; (b–e) grown from solutions containing progressively greater quantities of  $\text{MACl}$ ; (f–i) grown from solutions containing progressively greater quantities of  $\text{PbCl}_2$ . Adjacent images are grown from solutions with the same initial concentration of each species assuming complete solvation into discrete ions. (i) This is included purely to facilitate discussion. For a more complete representation of the morphological variety unique to the case of  $3\text{MAI} + \text{PbCl}_2$ , refer to Figure 1. All scale bars are  $1\ \mu\text{m}$ .

**Connecting Solution Chemistry to Nanoscale Crystal Development through TEM.** To gain more insight into the influence of chemistry on film formation, we developed a

sample preparation method that has allowed us to deposit and grow a perovskite film directly on a TEM grid under the same conditions used for device

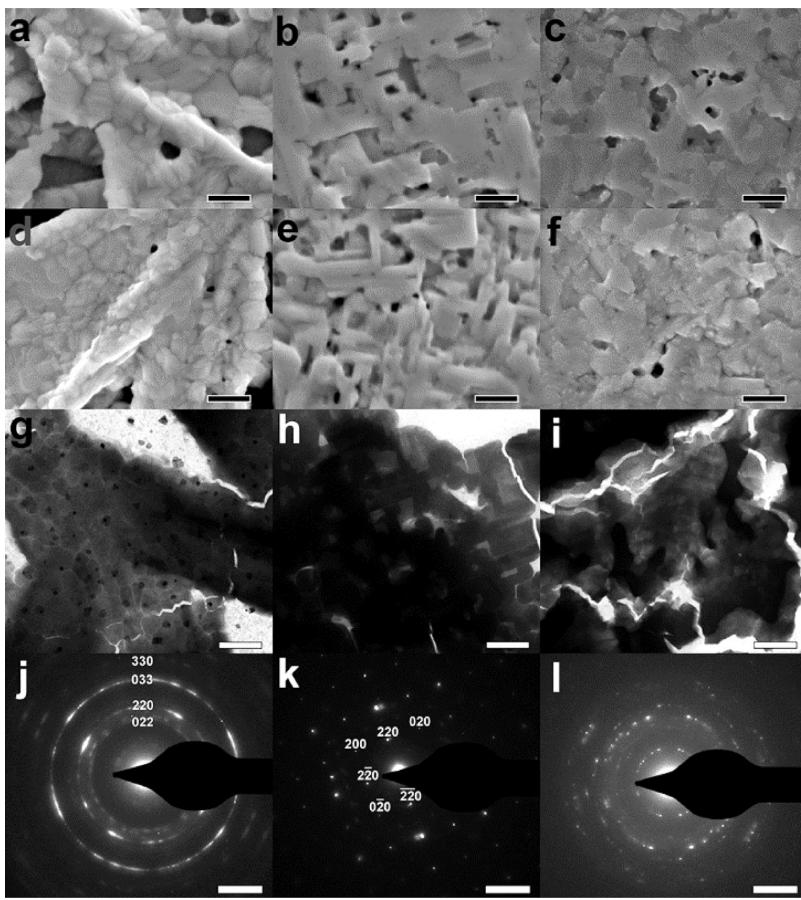


**Figure 3. Morphology and crystallographic texture of the three compositional extremes discussed.** (a–c) SEM and (d–f) TEM images of films grown from solutions of MAI + PbI<sub>2</sub> (left), 3MAI + PbCl<sub>2</sub> (middle), and 2MAI + MAI + PbI<sub>2</sub> (right). (g–i) Bright field TEM images taken of the films in (d–f) and (j–l) their corresponding select area electron diffractograms. Scale bars in (a–i) are 500 nm and scale bars in (j–l) are 2 nm<sup>−1</sup>.

fabrication. More detailed information on sample preparation can be found in the Methods section. The columns in Figure 3 correspond to films grown from MAI + PbI<sub>2</sub> (left), 3MAI + PbCl<sub>2</sub> (center), and MAI + 2MAI + PbI<sub>2</sub> (right) solutions, respectively. Figure 3a–f shows the morphological consistency achieved between systems grown conventionally and those fabricated on TEM grids. Figure 3g–i is the bright field TEM images of films formed from MAI + PbI<sub>2</sub>, 3MAI + PbCl<sub>2</sub>, and MAI + 2MAI + PbI<sub>2</sub>. Select area electron diffractograms (SAED) of the entire visible area in the bright field TEM images are shown in Figure 3j–l. All SAED patterns were indexed to the tetragonal MAPbI<sub>3</sub> phase observed to be stable at room temperature<sup>40,41</sup> with the aid of previously reported electron diffraction studies on oxide perovskite materials.<sup>42–44</sup>

As is immediately apparent in the clarity of the diffraction patterns, films formed from MAI + PbI<sub>2</sub> and 3MAI + PbCl<sub>2</sub> have differing crystallographic texture. In the MAI + PbI<sub>2</sub> film, we do find that grains tend to be oriented along the [111] zone axis (Supporting Information Figure S8a), but the diffraction pattern in Figure 3j somewhat replicates the distribution of peak

intensities of a fully disordered MAPbI<sub>3</sub> powder<sup>25</sup> demonstrating that growth under these conditions has a random character as well. In contrast, the 3MAI + PbCl<sub>2</sub> film's diffraction pattern (Figure 3k) appears like that of a single crystal. The sharp diffraction spots and the clarity of the pattern indicate long-range orientational coherence. This pattern is indexed to the [001] zone axis, but in 3MAI + PbCl<sub>2</sub> films, we observe large scale orientation along both the [001] and [100] zone axes with roughly equal frequency. The SAED pattern in Figure 3l suggests a relatively low tendency toward the generation of large scale crystallographic texture in the film grown from a solution of MAI + 2MAI + PbI<sub>2</sub>. That said, fine points replace the arcs in Figure 3j suggesting that while nucleation may proceed as it does in the case of MAI + PbI<sub>2</sub>, growth kinetics and thus crystallite size are altered. As has been mentioned periodically, the case of 3MAI + PbCl<sub>2</sub> is more complicated. Features of the 3MAI + PbCl<sub>2</sub> film that are epitomized by the morphologies of films formed from solutions of MAI + PbI<sub>2</sub> and MAI + 2MAI + PbI<sub>2</sub> can be seen and they display crystallographic texture similar to their analogues.

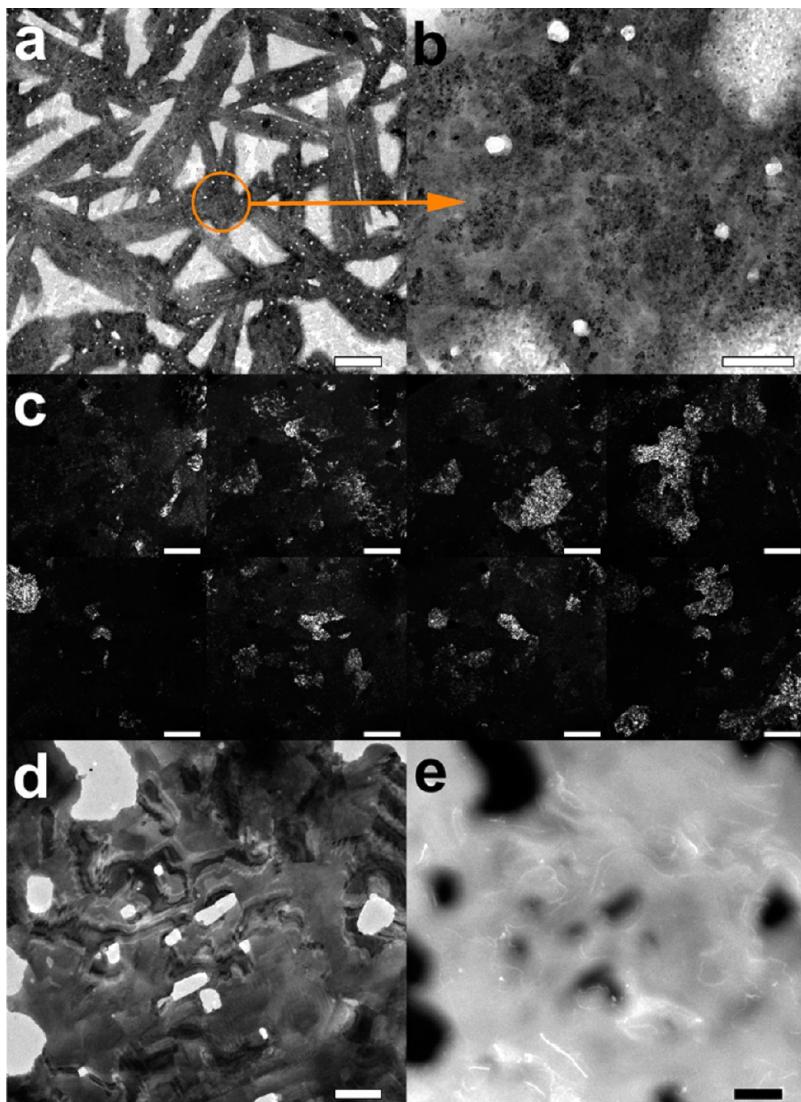


**Figure 4.** Comparison between the short-range order in films grown from  $\text{MAI} + \text{PbI}_2$  and the long-range lattice coherence in films grown from  $3\text{MAI} + \text{PbCl}_2$ . (a) Bright field image of a film grown from  $\text{MAI} + \text{PbI}_2$  (scale bar:  $1\ \mu\text{m}$ ) and (b) an image of the area indicated in (a) (scale bar:  $200\ \text{nm}$ ). (c) Eight dark field images of the region in (b) taken around the  $220$  and  $022$  diffraction rings. Scale bars are all  $200\ \text{nm}$ . (d) Bright field image of a film grown from a  $3\text{MAI} + \text{PbCl}_2$  solution, and (e) a dark field image of the same region representative of any of the region's diffraction spots which demonstrates orientational coherence at the micrometer length scale. Scale bars are both  $1\ \mu\text{m}$ .

The SAED patterns in Figure 3j–l reveals dramatic differences between collective crystal orientation in the three systems studied, but to get an idea of the grain structure within these systems we need to explore the information contained in the dark field. With the aid of an objective aperture, dark field imaging allows us to image the specific crystal domains responsible for creating particular diffraction signals in an SAED pattern. In Figure 4, we compare bright and dark field TEM images of films grown from  $\text{MAI} + \text{PbI}_2$  (Figure 4a–c) and  $3\text{MAI} + \text{PbCl}_2$  (Figure 4d,e). Figure 4c shows eight dark field images of the entire area shown in Figure 4b taken around the diffraction ring characteristic of  $\langle 220 \rangle$  reflections.

Each individual panel in Figure 4c shows crystallites that are roughly oriented with each other which serve

to outline what we term loosely as grains. We analyze a smaller area than that analyzed in the case of  $3\text{MAI} + \text{PbCl}_2$  (Figure 4d,e) because of the relatively small grain size. It should be noted that actual crystallite size indicated by the dark field analysis is on the  $2\text{–}20\ \text{nm}$  scale while the size of the grains they constitute are roughly an order of magnitude greater (Supporting Information Figure S8b). This may be another consequence of nucleation from the amorphous phase,<sup>45</sup> and is discussed more fully in the Supporting Information. Figure 4e is a representative dark field image of the area in Figure 4d taken at any of its diffraction spots as there is such great orientational coherence. Structure in Figure 4d approaches that of a single crystal. That said, contrast features visible in Figures 3h and 4d suggest many small crystallites rather than a large

single crystal. The long-range order maintained between what appear to be isolated crystallites is a key insight in unraveling the detailed mechanism of chloride's influence.

As is evident from the dark field images in Figure 4c, grain structure in the MAI + PbI<sub>2</sub> system has an average length scale that does not exceed ~200 nm while films grown from a 3MAI + PbCl<sub>2</sub> solution exhibit structural coherence, if not grain size itself, at or near the micrometer length scale. This clear long-range preservation of lattice coherence may provide a direct physical rational for the origin of the consistently observed but thus far poorly elucidated enhanced exciton diffusion length and lifetime in films grown from solutions with the stoichiometry 3MAI + PbCl<sub>2</sub>, and it may ground the enhancement in carrier lifetime observed by Stranks *et al.*<sup>24</sup> in the crystallographic consequences of chloride inclusion. While this is by no means the first suggestion of either increased orientation about the (100) axis or increased grain size as a result of chloride's presence,<sup>10,16,23</sup> it is the first time robust and direct links between common film morphologies and detailed crystallographic properties have been made.

The stark differences in texture between the three films (Figure 3j–l) indicate that both the presence and the chemical state of chloride species significantly affect the nature of the nucleation event, and this impact is preserved throughout film growth. The texture observed in the MAI + PbI<sub>2</sub> film about the [111] zone axis (Supporting Information Figure S8a), combined with the lack of orientational coherence between grains, indicates that nucleation at the substrate's surface is primarily driven by the interfacial energy between MAPbI<sub>3</sub> and PEDOT:PSS. This competes with perovskite nucleation from the amorphous phase noted by Park *et al.*<sup>45</sup> which produces random texture. In the case of the 3MAI + PbCl<sub>2</sub> film, the nucleation event is radically different as the texture observed in the MAI + PbI<sub>2</sub> film is largely absent. The case of the MAI + 2MACl + PbI<sub>2</sub> film seems to be intermediate between the two in which orientation about the [111] zone axis of the MAI + PbI<sub>2</sub> film is lost and the long-range coherence and selective orientation about the [100] and [001] zone axes of the 3MAI + PbCl<sub>2</sub> film is not achieved.

**Phase Evolution during Growth.** A greater understanding of phase development upon deposition and initial annealing is required in order to elucidate the mechanism of chloride modified crystal growth. To this end, the XRD patterns of films grown from 3MAI + PbCl<sub>2</sub> and MAI + 2MACl + PbI<sub>2</sub> solutions were characterized, both immediately after deposition and after 30 min of annealing at 90 °C (Supporting Information Figure S9). The most significant 2θ range was chosen for analysis to minimize the impact of the rapid transformation these unequilibrated films undergo upon exposure to the ambient conditions necessitated by the

measurement. A wider range is shown in Supporting Information Figure S10 for perspective. The primary phase components in Supporting Information Figure S9a,b are PbI<sub>2</sub>, MAPbI<sub>3</sub>, and what Colella *et al.* has characterized as a MAPbCl<sub>3</sub> phase,<sup>25</sup> which is unique to systems containing chloride. Tan *et al.* have also noted that this signal is unique to growth in the presence of chloride, and they have identified it as a crystalline precursor phase that plays an important role in film development.<sup>17</sup> Park *et al.* recently observed this phase in perovskite films grown on a mesoporous TiO<sub>2</sub> surface and they identified it as MAPbCl<sub>3</sub> as well.<sup>45</sup> Moore *et al.* echo this same sentiment, implicating this intermediate phase as a key component of growth in the presence of chloride.<sup>37</sup> At this point in the literature, the presence of this phase is clearly established, but its exact role in mediating transformation remains as of yet unclear. While current findings suggest that this phase may be more closely related to PbCl<sub>2</sub>,<sup>26</sup> have complex stoichiometry,<sup>27</sup> or be completely amorphous,<sup>46</sup> we will use the formula MAPbCl<sub>3</sub> to refer to this intermediate for ease and clarity. The range of order/disorder that the organo-lead iodide perovskite can support<sup>45</sup> suggests the possibility of similarly rich structural variety in its chloride analogue. Since these films are admittedly unstable under the conditions necessary for characterization, we attempted to compliment the observation of this phase through slowing film evolution and stabilizing intermediate phases by supplying the system with an amount of MAI in excess of both that required to form MAPbI<sub>3</sub> and that required to react with chloride ions (Figure 5), a process more thoroughly discussed by Yu *et al.*<sup>27</sup>

All of the systems presented in Figure 5 have been annealed for 2 h at 90 °C. As can be seen both in SEM and XRD (Figure 5a,d), the film with the composition 3MAI + PbI<sub>2</sub> never evolves much past the amorphous as-cast state<sup>13</sup> and exhibits no strong XRD signals. This demonstrates that the overburden of MAI greatly retards transformation to crystalline MAPbI<sub>3</sub> and MAPbI<sub>3-x</sub>Cl<sub>x</sub>,<sup>27</sup> as well as encouraging the persistence of the amorphous MAPbI<sub>3</sub> and MAPbI<sub>3-x</sub>Cl<sub>x</sub> phases noted by Park *et al.*<sup>45</sup> As we gradually replace PbI<sub>2</sub> with PbCl<sub>2</sub> we see morphological features begin to develop that are unique from what we have seen thus far (Figure 5b,c). If we consider the corresponding XRD patterns (Figure 5d), it becomes apparent that in the sample with the greatest PbCl<sub>2</sub> content (Figure 5c) features indicative of the intermediate phase discussed in Supporting Information Figure S9 can be observed (inset of Figure 5c). Both this phase and PbI<sub>2</sub> become more prominent as PbCl<sub>2</sub> is added to the system. At this point in the field, the importance of chloride loss<sup>27</sup> and the MAPbCl<sub>3</sub> intermediate<sup>27,37</sup> is reasonably well established, but the way these shape morphology and ultimate properties is still poorly understood.

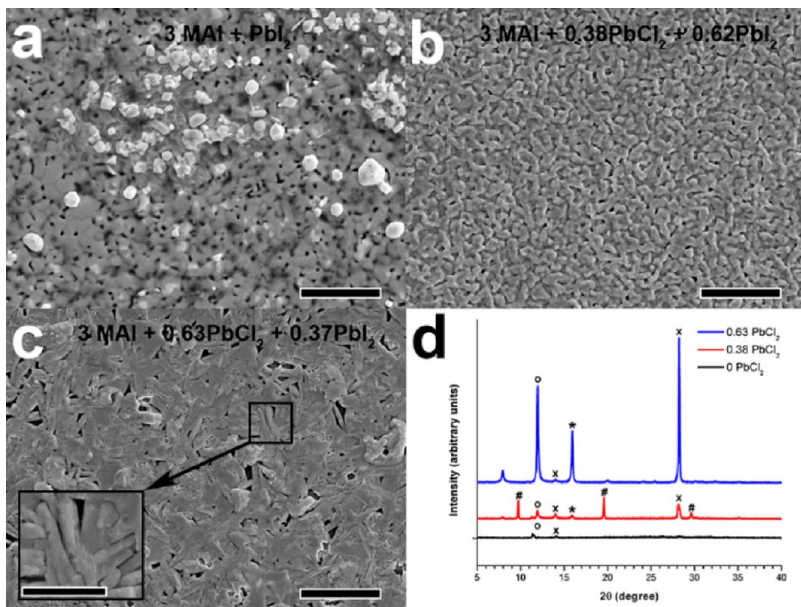


**Figure 5.** (a–c) Retarded film evolution in systems containing excess methylammonium; all scale bars are 5  $\mu\text{m}$  with the exception of the inset of (c) which is 2  $\mu\text{m}$ . (d) XRD patterns of (a–c), with ○ indicating  $\text{PbI}_2$ , x indicating  $\text{MAPbI}_3$ , \* indicating  $\text{MAPbCl}_3$ , and # indicating MAI. The inset in (c) shows what we suspect is the morphology of the  $\text{MAPbCl}_3$  intermediate.

To this end, scanning transmission electron microscopy (STEM) EDS was used to measure the spatial distribution of residual chloride in a 3MAI + PbCl<sub>2</sub> film annealed for only 80 min, 2/3 of typical annealing times (Supporting Information Figure S11). The bright field TEM image in Supporting Information Figure S11a is centered about a morphological feature analogous to that pointed out as MAPbCl<sub>3</sub> (inset of Figure 5c) caught mid-transformation. Residual chloride resides primarily at the center of this structure, suggesting this feature is indicative of the MAPbCl<sub>3</sub> phase, while the periphery is relatively iodide rich (Supporting Information Figures S11b,c). While instrument limitations required the map to be collected in sections, it can be seen that the halide composition gradient implies a reaction front moving from the outside in at which chloride is volatilized and replaced by iodide. As is evident near the top of Supporting Information Figure S11a, this is accompanied by structural changes which transform the bar like MAPbCl<sub>3</sub> intermediate into a morphology similar to Figure 1c through a templated self-assembly process.

**Influence of Dynamic Solution Equilibria.** These results demonstrate that the way chloride is introduced into the solution has an impact on ultimate film growth (as revealed in Figure 2), and thus that the complex ion equilibria in the precursor solution displayed in Figure 6 may play a nontrivial role in morphological development.<sup>47</sup> Using MACl and PbCl<sub>2</sub> to differentiate how chloride is introduced into the precursor solutions (Figure 2) has allowed us to enter this net of chemical equilibria at different points, highlighting the kinetic subtleties associated with seeking equilibrium in each case. By virtue of its integral role in the

self-assembly of the lead halide perovskite lattice, the presence of  $\text{MA}^+$  likely also plays an important role in these solution equilibria. Possibly, this goes as far as facilitating aggregation in solution reminiscent of the self-assembly that occurs upon deposition and annealing.

Despite limited knowledge of the exact aggregation that may form in solution and its relevant optical properties, dynamic light scattering was used to characterize particle size in freshly prepared solutions with stoichiometries 3MAI + PbCl<sub>2</sub> and MAI + 2MACl + PbI<sub>2</sub> (Supporting Information Figure S12). However, caution must be taken against a strictly quantitative interpretation of this data as arbitrary but consistent refractive indices were chosen for aggregates in the solutions. The more than an order of magnitude of difference in apparent aggregate size between the two systems is suggestive of the generation of solution based molecular order unique to each case. Although this technique is admittedly limited in interpreting what may be a broad distribution of aggregate compositions and sizes, the very recent work of Tidhar *et al.* provide direct evidence of solution phase aggregation through cryogenic TEM analysis.<sup>26</sup> They find that lead chloride crystallites naturally occur in the precursor solution, putting a face on what we can only characterize as aggregation at this stage. As since PbCl<sub>2</sub> is less soluble in DMF and the solutions are filtered before analysis, it is likely that the solution containing PbCl<sub>2</sub> has a slightly lower concentration of chloride. If this aggregation was formed from precipitation, this decreased chloride concentration should discourage aggregation not enhance it, yet we observe distinctly larger aggregate size in the case of the 3MAI + PbCl<sub>2</sub> solution. Thus, we offer

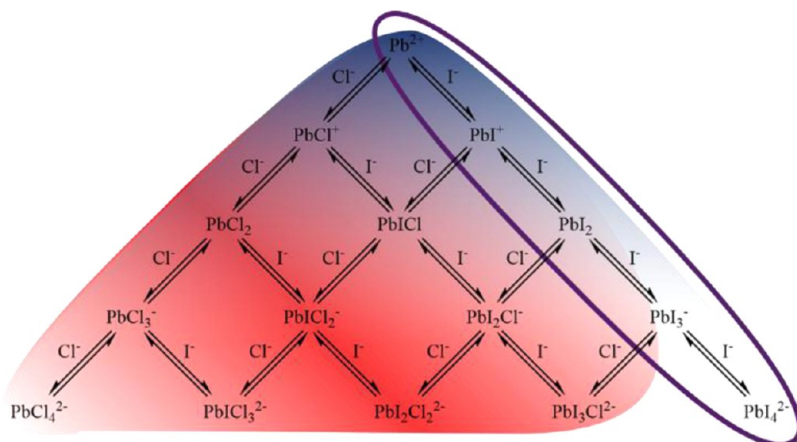


**Figure 6. Simultaneous complex ion equilibria in solutions containing lead, chloride, and iodide. Because of the poor solubility of  $\text{PbCl}_2$  and the excellent solubility of MAI in DMF, solutions with the stoichiometry  $3\text{MAI} + \text{PbCl}_2$  initially contain large concentrations of  $\text{I}^-$  and species near  $\text{PbCl}_2$  in this set of equilibria (red). Due to the good solubility of  $\text{PbI}_2$  in DMF, solutions with stoichiometries of both  $2\text{MAI} + \text{MAI} + \text{PbI}_2$  (blue) and  $\text{MAI} + \text{PbI}_2$  (circled) initially contain solvated halogen ions and species near  $\text{Pb}^{2+}$  in this set of equilibria.**

that the aggregation is kinetically driven and thus more dependent on the solvation process than on precipitation. As Dirin *et al.* has established that  $\text{MAPbI}_3$  readily serves as a lead chalcogenide nanoparticle ligand,<sup>47</sup> it is both likely that  $\text{MA}^+$  plays an important role in the kinetic control of this process and that the aggregation may be more compositionally complex than just  $\text{PbCl}_2$ .

This proposed link between chemical equilibria within the precursor solution and crystal evolution in the cast film helps rationalize the rich morphological variety observed in perovskite films fabricated from chloride containing solutions (Figure 1). These competing chemical processes do not reach equilibrium immediately or we would not observe such great differences between the films cast with the same overall stoichiometry in Figure 2. A given precursor solution likely continues to change subtly over time after it is made, impacting the nature of resulting perovskite films. To determine if such solution phase kinetics are important in controlling film development, we imaged a large area of a film cast from a freshly prepared solution of  $3\text{MAI} + \text{PbCl}_2$  and compared it with a film cast from a two week old solution of  $3\text{MAI} + \text{PbCl}_2$  (Supporting Information Figure S13a,b, respectively). As can be seen, both coverage and morphological distribution in these two films are quite disparate, with superior coverage being achieved through the use of the solution that was allowed to equilibrate for 2 weeks under inert atmosphere.

**Mechanism of Chloride's Impact on Crystallization.** From the importance of solution equilibria taken together with the stark differences in crystalline texture (Figure 3), the striking structural differences (Figure 4), and the formation/transformation of a chloride rich intermediate phase (Figures 5, Supporting Information Figures S9

and S11), we propose that while a simple self-assembly process directed by substrate interfacial energy drives the formation of  $\text{MAPbI}_3$  in films cast from  $\text{MAI} + \text{PbI}_2$ , a templated self-assembly process directed by the formation of a  $\text{MAPbCl}_3$  intermediate phase largely guides perovskite nucleation and growth in chloride containing systems (Figure 7). As shown schematically in Figure 7a,b, both the position of complex ion equilibria (Figure 6) and differences in solution based aggregation influence the morphology, orientation, and size of the chloride rich phase formed upon deposition. As is depicted in the enlarged regions in Figure 7c,  $\text{MA}^+$  and  $\text{I}^-$  then diffuse into these structural templates preceded by a reaction front where entropy gain from chloride volatilization (Scheme 1) and the stabilization of a newly established iodide rich phase propagates transformation onward.

The progress of this reaction front is likely accompanied by a certain degree of structural rearrangement to relieve stresses and to facilitate the continued sublimation of  $\text{MACl}$  or volatilization of  $\text{HCl}$  and methylamine gas, but from the orientational coherence observed in the SAED dark field analysis (Figures 3 and 4), it is apparent that this can proceed without inducing a significant loss of long-range order. This process is likely accompanied by continued but oriented nucleation of an iodide rich phase on exposed surfaces of the template phase which becomes preferential to nucleation on the substrate. We have labeled these phases as chloride rich and iodide rich in Figure 7 because we anticipate that the detailed phase evolution may be more complex than a simple and direct transformation. These findings are in good support of the topotactic transformation Moore *et al.* suggests may occur from a precursor phase to the desired lead iodide perovskite.<sup>37</sup> Taken together, the data presented in this study go further to suggest that it may be topotactic

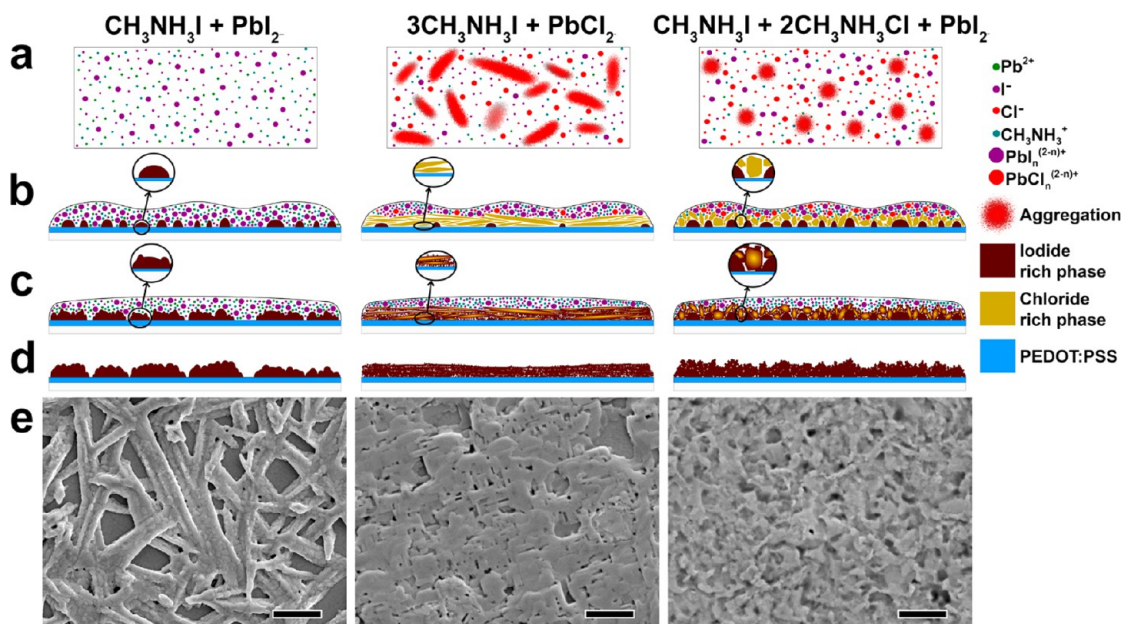


**Figure 7.** Simplified schematic representations of film formation in the three compositional extremes studied: (a) attempts to portray the state of the solution in each case. The sizes of aggregates represented in the cases of  $3\text{MAI} + \text{PbCl}_2$  and  $\text{MAI} + 2\text{MACl} + \text{PbI}_2$  are intended to differ by more approximately an order of magnitude. (b) illustration of nucleation during and immediately after deposition, (c) illustration of each system as it evolves during annealing, and (d) representation of the film morphology after annealing is complete. (e) SEM images representative of the morphologies illustrated schematically in (d). All scale bars are  $2\ \mu\text{m}$ . The case of  $3\text{MAI} + \text{PbCl}_2$  is highly idealized, and as previously discussed, a variety of morphologies are often observed together (Figure 1).

self-assembly of organo-lead iodide perovskite facilitated by the more structurally compatible chloride perovskite template phase that supports the generation of such unique long-range order in  $\text{CH}_3\text{NH}_3\text{PbI}_{3-x}\text{Cl}_x$ . The final morphology of each film system shown schematically in Figure 7d and empirically in Figure 7e preserves the structural framework built into it during initial deposition and rapid chloride rich phase growth. It should be noted that the case of  $3\text{MAI} + \text{PbCl}_2$  represented in Figure 7 is a simplification made to highlight the formation of the morphology we find to be unique to the case of films grown from solutions made with  $\text{PbCl}_2$ . Figure 8 shows a more realistic representation of film growth in the case of  $3\text{MAI} + \text{PbCl}_2$  in which we endeavor to show the link between the morphological variety we observe and the compositional gradients generated during rapid  $\text{MAPbCl}_3$  growth. These inhomogeneities in turn lead to continued nucleation and growth mediated by differing local chemistries throughout the film, with the three resulting extremes shown schematically in Figure 7.

This templated transformation likely bears a great deal in common with the transformation of  $\text{PbI}_2$  and/or  $\text{PbCl}_2$  into  $\text{MAPbI}_3$  or  $\text{MAPbI}_{3-x}\text{Cl}_x$  that occurs during the commonly employed two-step perovskite deposition.<sup>29,35,37</sup> In fact, Docampo *et al.* find that during the transformation from  $\text{PbI}_2$  to  $\text{MAPbI}_{3-x}\text{Cl}_x$  via immersion in an  $\text{MACl}$  isopropanol solution the same  $\text{MAPbCl}_3$  intermediate can be observed.<sup>29</sup>

Mechanistically understanding these transformations may prove to be key in the continuing rapid development of this material because of the role that both morphology and specific crystal orientation have been found to play in photophysical performance.<sup>35,36</sup> Haruyama *et al.* suggests that (110) and (001) terminations are preferentially conducive to hole transport<sup>36</sup> and Docampo *et al.* show that short circuit current increases alongside increasing orientation along the [100] axis.<sup>35</sup> Furthermore, they find that this orientation becomes increasingly dominant with increasing temperature which suggests that the templating influence of the  $\text{MAPbCl}_3$  phase dominates over transformation driven by  $\text{MAPbI}_3$  nucleation at higher temperatures. This is in keeping with Saliba *et al.*, who show that 2D XRD signals narrow when a short annealing step at  $130\ ^\circ\text{C}$   $\text{MAPbI}_{3-x}\text{Cl}_x$  follows deposition, indicating again that higher temperatures encourage preferential transformation through the  $\text{MAPbCl}_3$  intermediate.<sup>48</sup>

While the PEDOT:PSS based PHJ architecture has performed admirably (16.3% PCE),<sup>49</sup> the currently prevailing state of the art device is based on an inverted PHJ architecture in which perovskite is grown on yttrium doped  $\text{TiO}_2$  (19.3% PCE).<sup>50</sup> The close connection this study reveals between film morphology and actual crystal orientation gives us the means to extend this analysis to the wide breadth of literature focusing on  $\text{TiO}_2$  based architectures. Park *et al.* compare films grown from solutions of  $\text{MAI} + \text{PbI}_2$  and  $3\text{MAI} + \text{PbCl}_2$

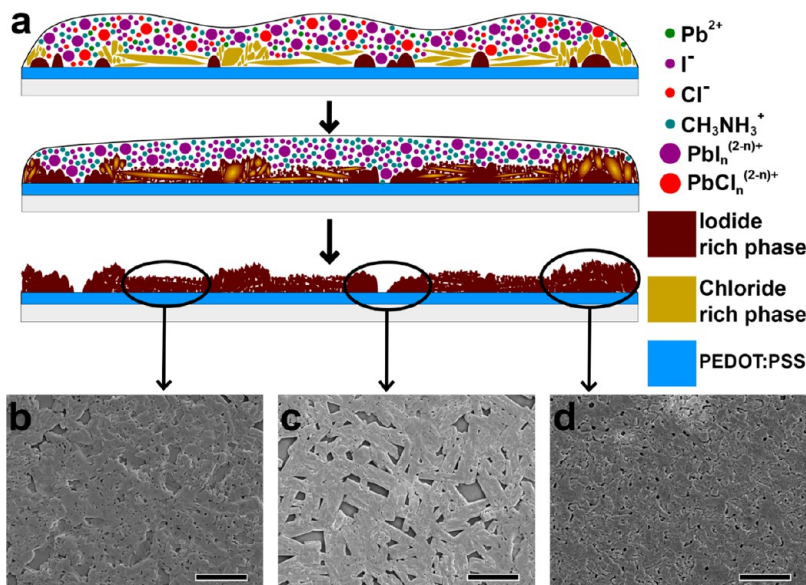


**Figure 8.** (a) A more realistic representation of nucleation during deposition (top), phase evolution and growth during annealing (middle), and final morphology (bottom) in the case of a film cast from a 3MAI +  $\text{PbCl}_2$  solution. (b–d) Images representative of the three major morphological constituents we observe in  $\text{MAPbI}_{(3-x)}\text{Cl}_x$  films grown on PEDOT:PSS from a 3MAI +  $\text{PbCl}_2$  solution (scale bars are  $5 \mu\text{m}$ ).

on mesoporous  $\text{TiO}_2$  and find that in the presence of chloride the morphology representative of Figure 8b dominates while the sharp hexagonal faceting in the film grown without chloride demonstrates likely orientation about the [111] axis.<sup>45</sup> This illustrates that the change in nucleation and thus ensuing growth behavior caused by chloride proceeds in the same manner on  $\text{TiO}_2$  as it does on PEDOT:PSS. Using comparable conditions, Eperon *et al.* and Zhao *et al.* demonstrate the formation of morphologies analogous to Figure 8, panels c and d, respectively, on a planar  $\text{TiO}_2$  interface.<sup>18,23</sup> Comparing these results<sup>18,23,45</sup> demonstrates that the same morphological variety observed here persists in systems based on  $\text{TiO}_2$ , suggesting that the dynamic solution processes discussed herein may play an analogous role. While not to neglect the important roles both the substrate<sup>26,51</sup> and thermal processing<sup>16,18,37,48</sup> play in morphological development, from the observations that in the presence of chloride on  $\text{TiO}_2$  crystal size increases,<sup>10,23</sup> crystallographic orientation along the [100] axis increases,<sup>10,16,23</sup> chloride all but completely volatilizes,<sup>26,27,29</sup> and an intermediate chloride perovskite phase is readily observable<sup>16,23,27,45</sup> it is possible that the same mechanism presented in Figures 7 and 8 may mediate perovskite film formation on  $\text{TiO}_2$ .

## CONCLUSION

In summary, we have elucidated the structural role chloride plays in the evolution of organo-lead halide perovskite films on PEDOT:PSS by establishing relationships between film morphology and subtle differences in precursor chemistry. We have expanded significantly upon this level of insight by developing a

sample preparation technique that enables the use of the TEM as an analytical tool to explore these systems. Because of the nature of the method, the findings are directly relevant to the low temperature solution processed PHJ devices currently being widely explored in the literature,<sup>10–20,49</sup> but we find that they may hold relevance for  $\text{TiO}_2$  based systems as well.<sup>10,16,18,23,26,27,29,45</sup>

From the sum total of the trends discussed herein, we offer that perovskite films grown from solutions containing chloride evolve through templated topo-tactic self-assembly in contrast to the conventional self-assembly prominent in films cast from MAI +  $\text{PbI}_2$ . Ultimately, this is due to a change in nucleation dynamics upon chloride inclusion as well as the existence of the unique and rapidly formed  $\text{MAPbCl}_3$  intermediate phase. The important role of chemical equilibria and aggregation in determining resulting morphology suggested by this study likely extends to most if not all other solution based perovskite preparations including those using additives<sup>13</sup> and mixed solvents<sup>52</sup> to enhance perovskite growth as well as those using other halogen anions,<sup>53</sup> organic cations,<sup>54</sup> and metal cations.<sup>55</sup> While these insights are of great engineering value, along the way we have established key relationships between nanoscale morphologies, textures, and grain structures unique to systems grown with and without chloride as well as a physical rationale for explaining the enhancement of carrier diffusion length in films fabricated from 3MAI +  $\text{PbCl}_2$ . Interfacial energy obviously plays a significant role in the development of these systems, and thus, this is a subject of continued investigation within our group. Solution rheology, annealing atmosphere, and proton equilibria within the solution and

deposited film are also important factors to consider when developing rational control of the morphological

evolution of these systems, and as such, work in these areas is underway.

## METHODS

**MAI and MACl Synthesis.** Methylammonium iodide (MAI) and methylammonium chloride (MACl) were synthesized by reacting 24 mL of 0.20 mol methylamine (33 wt % in absolute ethanol, Aldrich), 10 mL of 0.04 mol hydroiodic (57 wt % in water with 1.5% hypophosphorous acid, Alfa Aesar) or hydrochloric acid (37% in water, Aldrich), and 100 mL ethanol in a 250 mL round-bottom flask under nitrogen at 0 °C for 2 h with stirring. After reaction, the white precipitate of MAI or MACl was recovered by rotary evaporation at 40 °C and then dissolved in ethanol followed by sedimentation in diethyl ether by stirring the solution for 30 min. This step was repeated three times, and the MAI or MACl powder was finally collected and dried at 50 °C in a vacuum oven for 24 h.

**Perovskite Precursor Solution Preparation.** Perovskite precursor solutions were 20 wt % for TEM, STEM EDS, and DLS characterization and 40 wt % for SEM, EDS, XPS, and XRD measurements where **wt % = 100 × (total mass of solute/total mass of solution)**. The solutions were made in a nitrogen filled glovebox by mixing lead halide and methylammonium halide salts in anhydrous DMF in amounts appropriate to simultaneously achieve the stoichiometries noted in the text and the weight percent of solute required. Exact amounts are listed in Supporting Information Table S2 for all solutions studied assuming a constant volume of DMF (0.2 mL). The solutions were then stirred vigorously at 80 °C for ~40 min, cooled, and subsequently filtered through 0.45 μm PTFE filters.

**Fabrication of Perovskite Thin Films and TEM Samples.** ITO glass substrates were cleaned sequentially with detergent and deionized water, acetone, and isopropanol under sonication for 10 min. After drying under a N<sub>2</sub> stream, substrates were further cleaned by a plasma treatment for 30 s. PEDOT:PSS (Baytron P VP Al 4083, filtered through a 0.45 μm nylon filter) was first spin-coated onto the substrates at 5k rpm for 30 s and annealed at 150 °C for 10 min in air. To avoid oxygen and moisture, the substrates were transferred into a N<sub>2</sub>-filled glovebox, where the thin-film perovskite layers were spin-coated from a homogeneous 40 wt % perovskite precursor solution at 6k rpm for 45 s (300–500 nm thickness) and then annealed at 90 °C for 2–3 h.

TEM samples were prepared by first mounting a TEM grid on a cleaned ITO glass substrate. It is necessary to adhere an undistorted grid to the slide in slight tension with at minimum four points of contact to ensure intimate thermal contact. Otherwise, annealing conditions cannot be faithfully replicated. This can be done with any adhesive material with adequate solvent stability, adequate thermal stability, and adequately weak adhesion such that removal does not damage or distort the delicate TEM grid. Stronger tapes are more reliable but harder to work with without causing damage. To ensure appropriate PEDOT:PSS film formation, the grid's surface is made hydrophilic through glow discharge treatment with a Solarus 950 Gatan Advanced Plasma System. The same deposition and heat treatment procedure for first the PEDOT:PSS then the perovskite are then followed as above with the exception of the use of a 20 wt % precursor solution.

**Characterization.** A Tecnai G2 F20 transmission electron microscope was used at 200 kV for all TEM measurements. A FEI Sirion scanning electron microscope was used for all SEM based characterization with 5 kV used for imaging and 15 kV used for EDS. A Bruker D8 Focus powder diffractometer was used for all XRD characterization with a Cu K $\alpha$  source. A Versaprobe 5000 X-ray photoelectron spectrometer from Physical Electronics, Inc. was used for XPS measurements with a pass energy of 23.5 eV. A Malvern Instruments Ltd. ZEN3600 Zetasizer was used for DLS characterization.

**Conflict of Interest:** The authors declare no competing financial interest.

**Supporting Information Available:** Compositional data including SEM EDS, STEM EDS, and XPS as well as supplementary microscopy and XRD analysis. This material is available free of charge via the Internet at <http://pubs.acs.org>.

**Acknowledgment.** This material is based in part upon work supported by the State of Washington through the University of Washington Clean Energy Institute. The authors thank the support from the Air Force Office of Scientific Research (No. FA9550-09-1-0426), the Asian Office of Aerospace R&D (No. FA2386-11-1-4072), and the Office of Naval Research (No. N00014-14-1-246). A. K.-Y. Jen thanks the Boeing Foundation for support. S. T. Williams thanks the financial support from National Science Foundation Graduate Research Fellowship Program (No. DGE-1256082).

## REFERENCES AND NOTES

1. NCPV at NREL. Research Cell Efficiency Records. <http://www.nrel.gov/ncpv/> (accessed Sept 10, 2014).
2. Kojima, A.; Teshima, K.; Shirai, Y.; Miyasaka, T. Organometal Halide Perovskites as Visible-Light Sensitizers for Photovoltaic Cells. *J. Am. Chem. Soc.* **2009**, *131*, 6050–6051.
3. Kim, H.-S.; Lee, C.-R.; Im, J.-H.; Lee, K.-B.; Moehl, T.; Marchioro, A.; Moon, S.-J.; Humphry-Baker, R.; Yum, J.-H.; Moser, J. E.; et al. Lead Iodide Perovskite Sensitized All-Solid-State Submicron Thin Film Mesoscopic Solar Cell with Efficiency Exceeding 9%. *Sci. Rep.* **2012**, *2*, 591.
4. Wang, K.-C.; Jeng, J.-Y.; Shen, P.-S.; Chang, Y.-C.; Diau, E. W.-G.; Tsai, C.-H.; Chao, T.-Y.; Hsu, H.-C.; Lin, P.-Y.; Chen, P.; et al. P-Type Mesoscopic Nickel Oxide/Organometallic Perovskite Heterojunction Solar Cells. *Sci. Rep.* **2014**, *4*, 4756.
5. Ogomi, Y.; Kukihara, K.; Qing, S.; Toyoda, T.; Yoshino, K.; Pandey, S.; Momose, H.; Hayase, S. Control of Charge Dynamics through a Charge-Separation Interface for All-Solid Perovskite-Sensitized Solar Cells. *ChemPhysChem* **2014**, *15*, 1062–1069.
6. Kim, H. S.; Im, S. H.; Park, N.-G. Organolead Halide Perovskite: New Horizons in Solar Cell Research. *J. Phys. Chem. C* **2014**, *118*, 5615–5625.
7. Roldan-Carmona, C.; Malinkiewicz, O.; Soriano, A.; Espallargas, G. M.; Garcia, A.; Reinecke, P.; Kroyer, T.; Dar, M. I.; Nazeeruddin, M. K.; Bolink, H. J. Flexible High Efficiency Perovskite Solar Cells. *Energy Environ. Sci.* **2014**, *7*, 994–997.
8. Liu, D. Y.; Kelly, T. L. Perovskite Solar Cells with a Planar Heterojunction Structure Prepared Using Room-Temperature Solution Processing Techniques. *Nat. Photonics* **2014**, *8*, 133–138.
9. He, M.; Zheng, D. J.; Wang, M. Y.; Lin, C. J.; Lin, Z. Q. High Efficiency Perovskite Solar Cells: From Complex Nanostructure to Planar Heterojunction. *J. Mater. Chem. A* **2014**, *2*, 5994–6003.
10. Lee, M. M.; Teuscher, J.; Miyasaka, T.; Murakami, T. N.; Snaith, H. J. Efficient Hybrid Solar Cells Based on Mesosuperstructured Organometal Halide Perovskites. *Science* **2012**, *338*, 643–647.
11. Burschka, J.; Pellet, N.; Moon, S.-J.; Humphry-Baker, R.; Gao, P.; Nazeeruddin, M. K.; Grätzel, M. Sequential Deposition as a Route to High-Performance Perovskite-Sensitized Solar Cells. *Nature* **2013**, *499*, 316–319.
12. Chen, Q.; Zhou, H.; Hong, A.; Luo, S.; Duan, H.-S.; Wang, H.-H.; Liu, Y.; Li, G.; Yang, Y. Planar Heterojunction Perovskite Solar Cells via Vapor-Assisted Solution Process. *J. Am. Chem. Soc.* **2014**, *136*, 622–625.
13. Liang, P.-W.; Liao, C.-Y.; Chueh, C.-C.; Zuo, F.; Williams, S. T.; Xin, X.-K.; Lin, J.; Jen, A. K.-Y. Additive Enhanced Crystallization of Solution-Processed Perovskite for Highly

Efficient Planar-Heterojunction Solar Cells. *Adv. Mater.* **2014**, *26*, 3748–3754.

14. Ball, J. M.; Lee, M. M.; Hey, A.; Snaith, H. J. Low-Temperature Processed Meso-Superstructured to Thin-Film Perovskite Solar Cells. *Energy Environ. Sci.* **2013**, *6*, 1739–1743.

15. Carnie, M. J.; Charbonneau, C.; Davies, M. L.; Troughton, J.; Watson, T. M.; Wojciechowski, K.; Snaith, H. J.; Worsley, D. A. A One-Step Low Temperature Processing Route for Organoolead Halide Perovskite Solar Cells. *Chem. Commun.* **2013**, *49*, 7893–7895.

16. Dualeh, A.; Tétreault, N.; Moehl, T.; Gao, P.; Nazeeruddin, M. K.; Grätzel, M. Effect of Annealing Temperature on Film Morphology of Organic–Inorganic Hybrid Perovskite Solid-State Solar Cells. *Adv. Funct. Mater.* **2014**, *24*, 3250–3258.

17. Tan, K. W.; Moore, D. T.; Saliba, M.; Sai, H.; Estroff, L. A.; Hanrath, T.; Snaith, H. J.; Wiesner, U. Thermally Induced Structural Evolution and Performance of Mesoporous Block Copolymer-Directed Alumina Perovskite Solar Cells. *ACS Nano* **2014**, *8*, 4730–4739.

18. Eperon, G. E.; Burlakov, V. M.; Docampo, P.; Goriely, A.; Snaith, H. J. Morphological Control for High Performance, Solution-Processed Planar Heterojunction Perovskite Solar Cells. *Adv. Funct. Mater.* **2014**, *24*, 151–157.

19. Burlakov, V. M.; Eperon, G. E.; Snaith, H. J.; Chapman, S. J.; Goriely, A. Controlling Coverage of Solution Cast Materials with Unfavourable Surface Interactions. *Appl. Phys. Lett.* **2014**, *104*, 091602.

20. Heo, J. H.; Im, S.-H.; Noh, J. H.; Mandal, T. N.; Lim, C.-S.; Chang, J. A.; Lee, Y. H.; Kim, H.; Sarkar, A.; Nazeeruddin, M. K.; Grätzel, M.; et al. Efficient Inorganic–Organic Hybrid Heterojunction Solar Cells Containing Perovskite Compound and Polymeric Hole Conductors. *Nat. Photonics* **2013**, *7*, 486–492.

21. Liu, M. Z.; Johnston, M. B.; Snaith, H. J. Efficient Planar Heterojunction Perovskite Solar Cells by Vapour Deposition. *Nature* **2013**, *501*, 395–398.

22. Edri, E.; Kirmayer, S.; Kulbak, M.; Hodes, G.; Cahen, D. Chloride Inclusion and Hole Transport Material Doping to Improve Methyl Ammonium Lead Bromide Perovskite-Based High Open-Circuit Voltage Solar Cells. *J. Phys. Chem. Lett.* **2014**, *5*, 429–433.

23. Zhao, Y.; Zhu, K.  $\text{CH}_3\text{NH}_3\text{Cl}$ -Assisted One-Step Solution Growth of  $\text{CH}_3\text{NH}_3\text{PbI}_3$ : Structure, Charge-Carrier Dynamics, and Photovoltaic Properties of Perovskite Solar Cells. *J. Phys. Chem. C* **2014**, *118*, 9412–9418.

24. Stranks, S. D.; Eperon, G. E.; Grancini, G.; Menelaou, C.; Alcocer, M. J. P.; Leijtens, T.; Herz, L. M.; Petrozza, A.; Snaith, H. J. Electron–Hole Diffusion Lengths Exceeding 1 Micrometer in an Organometal Trihalide Perovskite Absorber. *Science* **2013**, *342*, 341–344.

25. Colella, S.; Mosconi, E.; Fedeli, P.; Listorti, A.; Gazza, F.; Orlandi, F.; Ferro, P.; Besagni, T.; Rizzo, A.; Calestani, G.; et al.  $\text{MAPbI}_{3-x}\text{Cl}_x$  Mixed Halide Perovskite for Hybrid Solar Cells: The Role of Chloride as Dopant on the Transport and Structural Properties. *Chem. Mater.* **2013**, *25*, 4613–4618.

26. Tidhar, Y.; Edri, E.; Weissman, H.; Zohar, D.; Hodes, G.; Cahen, D.; Rybtchinski, B.; Kirmayer, S. Crystallization of Methyl Ammonium Lead Halide Perovskites: Implications for Photovoltaic Applications. *J. Am. Chem. Soc.* **2014**, *10.1021/ja505556s*.

27. Yu, H.; Wang, F.; Xie, F.; Li, W.; Chen, J.; Zhao, N. The Role of Chlorine in the Formation Process of “ $\text{CH}_3\text{NH}_3\text{PbI}_{3-x}\text{Cl}_x$ ” Perovskite. *Adv. Funct. Mater.* **2014**, *10.1002/adfm.201401872*.

28. You, J.; Hong, Z.; Yang, Y. M.; Chen, Q.; Cai, M.; Song, T.-B.; Chen, C.-C.; Lu, S.; Liu, Y.; Zhou, H.; et al. Perovskite Solar Cells with High Efficiency and Flexibility. *ACS Nano* **2014**, *8*, 1674–1680.

29. Docampo, P.; Hanusch, F.; Stranks, S. D.; Döblinger, M.; Feckl, J. M.; Ehrensparger, M.; Minar, N. K.; Johnston, M. B.; Snaith, H. J.; Bein, T. Solution Deposition-Conversion for Planar Heterojunction Mixed Halide Perovskite Solar Cells. *Adv. Energy Mater.* **2014**, *4*, No. 1400355.

30. Olszak-Humienik, M. On the Thermal Stability of Some Ammonium Salts. *Thermochim. Acta* **2001**, *378*, 107–112.

31. Yamamoto, O.; Oguni, M.; Matsuo, T.; Suga, H. P-T Phase Relations of Methylammonium Halides. *Thermochim. Acta* **1986**, *98*, 327–338.

32. Niu, G.; Li, W.; Meng, F.; Wang, L.; Dong, H.; Qiu, Y. Study on the Stability of  $\text{CH}_3\text{NH}_3\text{PbI}_3$  Films and the Effect of Post-Modification by Aluminum Oxide in All-Solid-State Hybrid Solar Cells. *J. Mater. Chem. A* **2014**, *2*, 705–710.

33. Even, J.; Pedesseau, L.; Katan, C. Analysis of Multivalley and Multibandgap Absorption and Enhancement of Free Carriers Related to Exciton Screening in Hybrid Perovskites. *J. Phys. Chem. C* **2014**, *118*, 11566–11572.

34. Du, M. H. Efficient Carrier Transport in Halide Perovskites: Theoretical Perspectives. *J. Mater. Chem. A* **2014**, *2*, 9091–9098.

35. Docampo, P.; Hanusch, F. C.; Giesbrecht, N.; Angloher, P.; Ivanova, A.; Bein, T. Influence of the Orientation of Methylammonium Lead Iodide Perovskite Crystals on Solar Cell Performance. *APL Mater.* **2014**, *2*, 081508.

36. Haruyama, J.; Sodeyama, K.; Han, L.; Tateyama, Y. Termination Dependence of Tetragonal  $\text{CH}_3\text{NH}_3\text{PbI}_3$  Surfaces for Perovskite Solar Cells. *J. Phys. Chem. Lett.* **2014**, *5*, 2903–2909.

37. Moore, D. T.; Sai, H.; Wee Tan, K.; Estroff, L. A.; Wiesner, U. Impact of the Organic Halide Salt on Final Perovskite Composition for Photovoltaic Applications. *APL Mater.* **2014**, *2*, 081802.

38. Clever, H. L.; Johnston, F. J. The Solubility of Some Sparingly Soluble Lead Salts: An Evaluation of the Solubility in Water and Aqueous Electrolyte Solution. *J. Phys. Chem. Ref. Data* **1980**, *9*, 751–784.

39. Horváth, O.; Mikó, I. Spectra, Equilibrium and Photoredox Chemistry of Tri- and Tetraiodoplumbate(II) Complexes in Acetonitrile. *J. Photochem. Photobiol. A* **1998**, *114*, 95–101.

40. Stoumpos, C. C.; Malliakas, C. D.; Kanatzidis, M. G. Semiconducting Tin and Lead Iodide Perovskites with Organic Cations: Phase Transitions, High Mobilities, and Near-Infrared Photoluminescent Properties. *Inorg. Chem.* **2013**, *52*, 9019–9038.

41. Poglitsch, A.; Weber, D. Dynamic Disorder in Methylammoniumtrihalogenoplumbates(II) Observed by Millimeter-Wave Spectroscopy. *J. Chem. Phys.* **1987**, *87*, 6373–6378.

42. Otonicar, M.; Skapin, S. D.; Jancar, B.; Ubic, R.; Suvorov, D. Analysis of the Phase Transition and the Domain Structure in  $\text{K}_{0.5}\text{Bi}_{0.5}\text{TiO}_3$  Perovskite Ceramics by *in Situ* XRD and TEM. *J. Am. Ceram. Soc.* **2010**, *93*, 4168–4173.

43. Woodward, D. I.; Reaney, I. M. Electron Diffraction of Tilted Perovskites. *Acta Crystallogr.* **2005**, *61*, 387–399.

44. Keller, L. P.; Buseck, P. R. Twinning in Meteoritic and Synthetic Perovskite. *Am. Mineral.* **1994**, *79*, 73–79.

45. Park, B.-W.; Philippe, B.; Gustafsson, T.; Sveinbjörnsson, K.; Hagfeldt, A.; Johansson, E. M. J.; Boschloo, G. Enhanced Crystallinity in Organic–Inorganic Lead Halide Perovskites on Mesoporous  $\text{TiO}_2$  via Disorder–Order Phase Transition. *Chem. Mater.* **2014**, *26*, 4466–4471.

46. Grätzel, M. The Light and Shade of Perovskite Solar Cells. *Nat. Mater.* **2014**, *13*, 838–842.

47. Dirin, D. N.; Dreyfuss, S.; Bodnarchuk, M. I.; Nedelcu, G.; Papagiorgis, P.; Itskos, G.; Kovalenko, M. V. Lead Halide Perovskites and Other Metal Halide Complexes as Inorganic Capping Ligands for Colloidal Nanocrystals. *J. Am. Chem. Soc.* **2014**, *136*, 6550–6553.

48. Saliba, M.; Tan, K. W.; Sai, H.; Moore, D. T.; Scott, T.; Zhang, W.; Estroff, L. A.; Wiesner, U.; Snaith, H. J. The Influence of Thermal Processing Protocol upon the Crystallization and Photovoltaic Performance of Organic–Inorganic Lead Trihalide Perovskites. *J. Phys. Chem. C* **2014**, *118*, 17171–17177.

49. Wu, C.-G.; Chiang, C.-H.; Tseng, Z.-L. Planar Heterojunction Perovskite/PC<sub>71</sub>BM Solar Cells with Enhanced Open-Circuit Voltage via (2/1)-Step Spin-Coating Process. *J. Mater. Chem.* **2014**, *2*, 15897–15903.

50. Zhou, H.; Chen, Q.; Li, G.; Luo, S.; Song, T.-B.; Duan, H.-S.; Hong, Z.; You, J.; Liu, Y.; Yang, Y. Interface Engineering of Highly Efficient Perovskite Solar Cells. *Science* **2014**, *345*, 542–546.

51. De Bastiani, M.; D'Innocenzo, V.; Stranks, S. D.; Snaith, H. J.; Petrozza, A. Role of the Crystallization Substrate on the Photoluminescence Properties of Organo-Lead Mixed Halides Perovskites. *Appl Mater.* **2014**, *2*, 081509.
52. Kim, H.-B.; Choi, H.; Jeong, J.; Kim, S.; Walker, B.; Song, S.; Kim, J. Y. Mixed Solvents for the Optimization of Morphology in Solution-Processed, Inverted-Type Perovskite/Fullerene Hybrid Solar Cells. *Nanoscale* **2014**, *6*, 6679–6683.
53. Edri, E.; Kirmayer, S.; Cahen, D.; Hodes, G. High Open-Circuit Voltage Solar Cells Based on Organic–Inorganic Lead Bromide Perovskite. *J. Phys. Chem. Lett.* **2013**, *4*, 897–902.
54. Pang, S.; Hu, H.; Zhang, J.; Lv, S.; Yu, Y.; Wei, F.; Qin, T.; Xu, H.; Liu, A.; Cui, G.  $\text{NH}_2\text{CH}=\text{NH}_2\text{PbI}_3$ : An Alternative Organo-lead Iodide Perovskite Sensitizer for Mesoscopic Solar Cells. *Chem. Mater.* **2014**, *26*, 1485–1491.
55. Hao, F.; Stoumpos, C. C.; Cao, D. H.; Chang, R. P. H.; Kanatzidis, M. G. Lead-Free Solid-State Organic–Inorganic Halide Perovskite Solar Cells. *Nat. Photonics* **2014**, *8*, 489–494.